Preprint CheMIn Technical Reports ISSN 3061-1075

Assembly Modelling of Cyclic and Prismatic Polyoxoaurates

Aleksandar Kondinski [1]

released: 5 August 2026

[1] Institute of Physical and
Theoretical Chemistry
Graz University of Technology
Stremayrgasse 9, 8010 Graz, Austria

Preprint No. 6



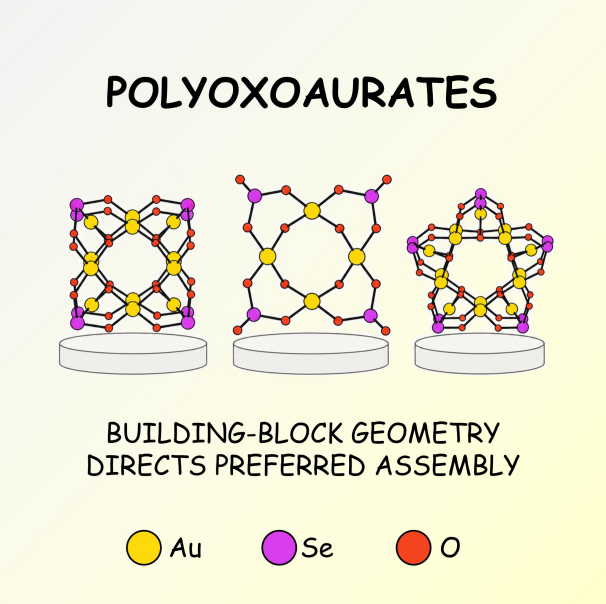
Keywords: polyoxometalates, polyoxoaurates, density functional theory, geometric strain, electronic structure

Edited by
Chemical Modelling and Informatics Group
Institute of Physical and Theoretical Chemistry
Graz University of Technology
Stremayrgasse 9, 8010 Graz
Austria (Europe)

E-Mail: kondinski@tugraz.at
World Wide Web: http://chemin.at/

Abstract

Polyoxometalates are discrete metal oxo clusters built from linked metal oxygen coordination units. Here, we use assembly modelling and density functional theory to examine two polyoxoselenitoaurate families, $[AuSeO_4]_n^{n-}$ and $[Au_3Se_2O_8]_n^{n+}$, with $n = 2$ to 6. Both families are constructed from $\{AuO_4\}$ square planar and $\{SeO_3\}$ trigonal pyramidal building units, allowing cyclic and prismatic architectures to be compared directly. The results show that stability is governed by how well each nuclearity accommodates the local geometry of these units. The cyclic tetramer best preserves the Au–O geometry, whereas the pentagonal prismatic cage is lowest in energy among the prismatic structures, closely followed by the cubic tetramer. Alternative selenite orientations are destabilised by short nonbonding O···O contacts and geometric congestion. Both families are closed shell and show HOMO–LUMO gaps of about 3.2 to 3.9 eV. The calculated trends rationalise the experimentally observed nuclearities and identify local geometric strain as a design principle for polyoxoaurate synthesis.



Highlights

- Assembly modelling of cyclic and prismatic polyoxoaurates (n = 2–6).
- The cyclic tetramer best preserves square-planar Au–O coordination geometry.
- The pentagonal-prismatic cage is the lowest-energy prismatic structure.
- Local geometric strain rationalises the observed polyoxoaurate nuclearities.

Contents

1 Introduction **3**

2 Methodology **4**

3 Results and Discussion **5**

3.1 Topological and Geometric Properties 5

3.2 Relative Stability and Electronic Properties 8

4 Conclusions **11**

A Tables **13**

B POMAssembler workflow and comparison with conventional builders **20**

C Notes on the electronic-structure analysis **20**

D Optimised Geometries **21**

References **24**

1 Introduction

Polyoxometalates (POMs) constitute a broad family of metal–oxo clusters with important applications in catalysis [25], biomedicine [3, 10, 42], and nanoelectronics [16, 21]. Most classical POM chemistry is dominated by early transition metals such as V, Nb, Ta, Mo, and W, yet late-transition-metal and actinide oxo clusters also display rich structural diversity [18, 30]. A useful survey of structural and electronic diversity among late-transition-metal and noble-metal polyoxometalates has been provided by Putaj and Lefebvre [39] and, in a broader review covering noble metals as POM constituents, by Izarova, Pope, and Kortz [12]. Frameworks such as Keggin [19], Lindqvist [24], and Anderson–Evans [4] continue to serve as reference motifs for understanding how local coordination preferences propagate into larger architectures. Continued advances in crystal engineering [8, 28] and molecular design [13, 23, 54] have further broadened the range of accessible structures and functions. Computational studies have also become central for connecting POM structure with bonding, counter-cation effects, protonation, and reactivity [9, 26, 27, 43].

Gold-based polyoxoaurates occupy a particularly interesting position within this landscape. The first polyoxoaurate, $(H_3O)_2[Au_{12}O_8(SeO_3)_8](HSeO_4)_6$, was obtained from the reaction of metallic gold with concentrated selenic acid at elevated temperature in sealed glass ampoules [5]. Its cationic cluster core, $[Au_{12}O_8(SeO_3)_8]^{4+}$, features a cuboctahedral Au framework supported by oxide and selenite ligands. Under related conditions $[Au_{15}O_{10}(SeO_3)_{10}]^{5+}$ was also isolated, containing a fivefold-capped pentagonal-prismatic gold arrangement [5]. In both systems the Au atoms are held together not by direct metal–metal bonding as the dominant structural element, but by an extended oxide/selenite scaffold. A further discrete, fully inorganic polyoxoaurate, $[Au^{III}_4As^{V}_4O_{20}]^{8-}$, was subsequently isolated in aqueous medium and confirmed that small, well-defined $\{AuO_4\}$-based clusters can be obtained as molecular species [11]. These compounds also highlight the structural kinship between polyoxoaurates and other late-transition-metal oxo clusters, including polyoxocuprates [14], polyoxopalladates and polyoxonickelates [6], as well as palladium selenito-oxo clusters [7].

A particularly relevant benchmark is the discrete polyoxoselenitoaurate $[Au^{III}_4O_4(Se^{IV}O_3)_4]^{4-}$, isolated in aqueous medium under ambient conditions [51]. This compound established that comparatively small and well-defined Au/Se/O assemblies can exist as discrete molecular species. Subsequent time-dependent DFT and electrospray mass spectrometry studies on this and related species clarified both their solution behaviour and their electronic structure [20]. Together, these observations motivate a systematic examination of how the same $\{AuO_4\}$ and $\{SeO_3\}$ building blocks accommodate different nuclearities, and why some assemblies are favoured while others are destabilised by accumulated strain.

In the present work we address this question by examining the $[AuSeO_4]^{n-}_n$ and $[Au_3Se_2O_8]^{n+}_n$ series for $n = 2$–6. The first family corresponds to bent ring-type architectures, whereas the second gives compact cage-type assemblies, as illustrated in Fig. 1. Because both families are built from nearly ideal $\{AuO_4\}$ square-planar and $\{SeO_3\}$ trigonal-pyramidal units, they provide a controlled platform for analysing how nuclearity, topology, and local strain are related. Gold remains in the $+3$ oxidation state throughout. The clusters are closed-shell and diamagnetic, and the absence of dominant metal–metal bonding sim-

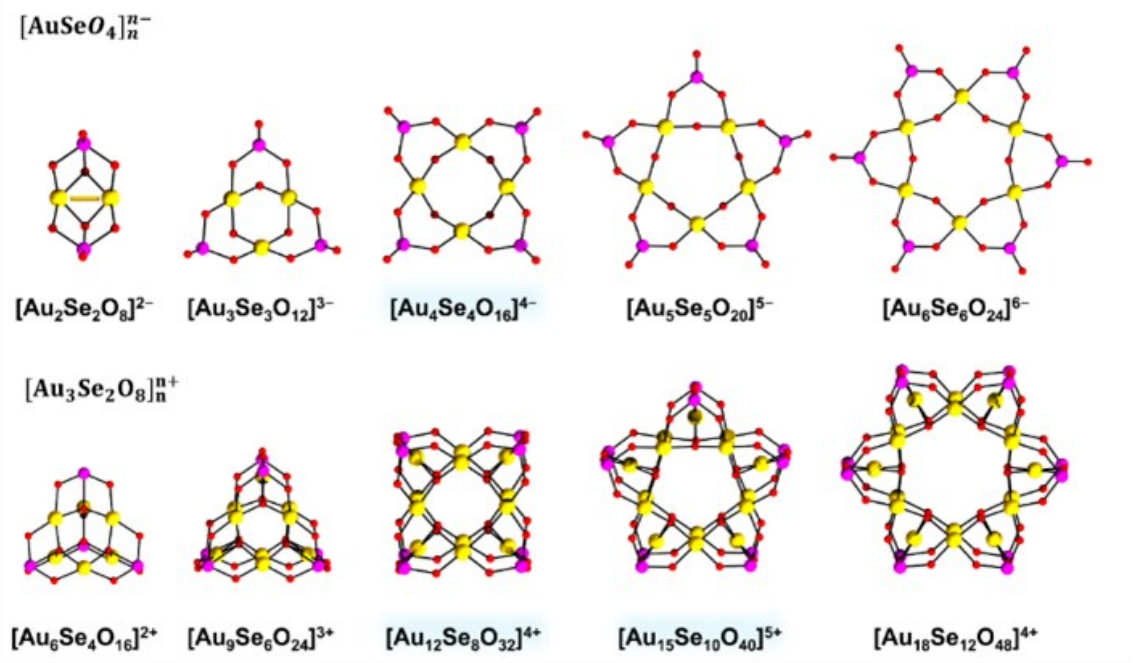


Figure 1: *Representative ring-type (top) and cage-type (bottom) polyoxoaurate models for $n = 2$–6. Au is yellow, Se violet, and O red. Grey shading marks experimentally observed members.*

plifies interpretation. Under these conditions, deviations in bond angles, non-bonding contacts, and relative energies can be linked directly to the geometric demands of assembly. Beyond rationalising the known polyoxoaurate nuclearities, the results offer a transferable criterion—local coordination strain—for screening candidate POM-based architectures, including noble-metal-substituted frameworks and extended hybrid materials.

2 Methodology

Initial geometries for all members of both series were generated with POMAssembler, a topology-based rigid-block construction code extending an earlier assembler for metal–organic polyhedra [22], developed for this work and freely available under the MIT licence [17]. The program differs from conventional model builders in that it does not rely on experimental fragments or manual atom-by-atom assembly; instead, it encodes a target architecture as a set of shared Au connector sites and a set of block-placement slots. Each slot specifies which connector sites are occupied by a rigid building block and defines an outward direction used to orient the selenite group. This makes it straightforward to scan nuclearities and topologies while preserving the local geometry of the constituent units. Two input fragments were used: a two-connector $\{\mathrm{Au–SeO_3–Au}\}$ block for the $[\mathrm{AuSeO_4}]_n^{n-}$ ring-type series and a three-connector $\{\mathrm{Au_3–SeO_3}\}$ block for the $[\mathrm{Au_3Se_2O_8}]_n^{n+}$ cage-type series. A more detailed description of the algorithm, including the treatment of connector merging and sanitisation, is given in the Supporting Information.

For the cyclic $[AuSeO_4]_n^{n-}$ structures, the two-connector block was placed on the edges of a regular n-gon, with the Au–Au connector axis aligned to each polygon edge and the $\{SeO_3\}$ unit directed radially outward. For the special $n = 2$ member of the cage series, four three-connector blocks were placed on alternating triangular faces of an octahedral Au scaffold. For the prismatic cage members with $n = 3$–6, an abstract n-gonal prism was used to define the Au scaffold: shared Au positions were placed at the centres of the top, bottom, and vertical prism edges, giving $3n$ Au sites. Each prism vertex is incident to three edges, and the corresponding three edge-centre positions define one triangular slot for an $\{Au_3–SeO_3\}$ block. Thus, each prismatic cage is assembled from $2n$ such blocks.

Rigid placement was performed by aligning connector atoms to their target sites. Two-connector blocks were aligned by matching the connector axis and the outward direction, whereas three-connector blocks were fitted by Kabsch alignment of the Au connector atoms with an additional outward-orientation constraint. After placement, coincident Au atoms and overlapping oxygen atoms at shared junctions were merged or sanitised to give chemically reasonable starting coordinates. These assembled structures were used only as input geometries for subsequent DFT optimisation. The final geometries and energetic trends discussed below are those obtained from the quantum-chemical calculations.

Geometry optimisations were performed with the Amsterdam Density Functional (ADF) package (version 2017) [41, 44] using the BP86 Generalised Gradient Approximation (GGA) functional [47, 48] with triple-zeta plus polarisation (TZP) Slater-type basis sets [45]. Scalar relativistic effects were included via the zero-order regular approximation (ZORA) [46], and solvent effects were represented by the conductor-like screening model (COSMO) with water as solvent [15, 40]. All optimised structures are closed-shell singlets.

Single-point calculations on the optimised geometries were performed at the B3LYP/TZP/ZORA-scalar/COSMO-water level (hybrid exchange-correlation functional with 20% exact exchange) to obtain frontier-orbital energies, HOMO–LUMO gaps, bonding energies per repeating unit, atomic-orbital population analyses, and Hirshfeld atomic charges. These data are reported in the Supporting Information.

3 Results and Discussion

3.1 Topological and Geometric Properties

The reliability of the computational protocol was assessed by comparison with the experimentally known members of both series. For the ring-type tetramer $[AuSeO_4]_4^{4-}$, the calculated bond lengths are Se–O_t = 1.680 Å, Se–O_b = 1.816 Å, and Au–O = 2.010–2.053 Å. For the experimentally known cage-type structures $[Au_3Se_2O_8]_4^{4+}$ and $[Au_3Se_2O_8]_5^{5+}$, the calculated Se–O and Au–O distances are likewise consistent with the reported crystal data (see Supporting Information, Table S1, for the complete set of characteristic bond lengths). This agreement supports extending the same theoretical level to the neighbouring nuclearities.

The $[AuSeO_4]_n^{n-}$ members with $n = 3$–6 are bent rings of corner-sharing $\{AuO_4\}$ square planes linked by μ_2-$\{SeO_3\}$ groups. The dimer $[AuSeO_4]_2^{2-}$ is structurally distinct: its two

Table 1: *Representative O–Au–O angular descriptors for the optimised ring-type and cage-type polyoxoaurates. For the $n = 3$, $n = 5$, and $n = 6$ cage structures two inequivalent Au sites are present; both are listed.*

System	∠O–Au–O_{out} (°)	∠O–Au–O_{in} (°)	∠O–Au–$O_{o/in}$ (°)
$[AuSeO_4]_2^{2-}$	97.0	78.9	84.6
$[AuSeO_4]_3^{3-}$	95.1	93.6	85.4
$[AuSeO_4]_4^{4-}$	87.2	93.3	89.7
$[AuSeO_4]_5^{5-}$	81.2	90.3	94.0
$[AuSeO_4]_6^{6-}$	80.6	85.6	96.7
$[Au_3Se_2O_8]_2^{2+}$	119.6	93.1	73.7
$[Au_3Se_2O_8]_3^{3+}$, ring Au	101.5	84.6	86.6
$[Au_3Se_2O_8]_3^{3+}$, belt Au	100.8	84.9	87.2
$[Au_3Se_2O_8]_4^{4+}$	89.6	84.4	93.0
$[Au_3Se_2O_8]_5^{5+}$, ring Au	81.2	85.4	96.7
$[Au_3Se_2O_8]_5^{5+}$, belt Au	82.3	86.1	95.8
$[Au_3Se_2O_8]_6^{6+}$, ring Au	75.7	88.5	97.8
$[Au_3Se_2O_8]_6^{6+}$, belt Au	77.8	87.6	97.3

$\{AuO_4\}$ units are edge-sharing rather than corner-sharing, and the Au$\cdots$Au separation contracts to approximately 2.55 Å—consistent with incipient aurophilic interaction and markedly shorter than the non-bonding Au$\cdots$Au contacts in the larger ring members. In all cases the rings are non-planar. Because each $\{SeO_3\}$ pyramid may point to either side of the bent ring, multiple configurational isomers are possible. The lowest-energy structures are those that best avoid short non-bonding contacts in the congested inner region of the ring (see Section 3.2).

A convenient strain measure in the ring series is provided by three O–Au–O angular descriptors: the outside angle, the inside angle, and the mixed outside/inside angle, defined schematically in Fig. 2 and quantified in Table 1 (see also Supporting Information, Table S2, for the ring inter-plane dihedral and Se–O–Se angles). The tetramer shows the most balanced local geometry (87.2°, 93.3°, and 89.7°, respectively), close to the ideal 90° of square-planar coordination. The trimer and pentamer remain reasonably close to this ideal, whereas the dimer (97.0°, 78.9°, 84.6°) and hexamer (80.6°, 85.6°, 96.7°) deviate substantially.

The interatomic distances (Supporting Information, Table S3) quantify how ring strain redistributes with nuclearity. Going from the tetramer to the pentamer and hexamer, the outer O$\cdots$O contacts contract from 2.832 to 2.677 and 2.661 Å, while the side O$\cdots$O distances lengthen from 2.865 to 2.980 and 3.048 Å, and the Se$\cdots$Se separation decreases from 6.223 to 6.031 and 5.814 Å. Ring expansion beyond the tetramer therefore does not produce a simply larger, flatter wheel. Instead, it narrows the outer and inner rims while thickening the ring laterally. The tetramer is preferred because it offers the most balanced compromise between ring closure and local square-planar coordination.

The $[Au_3Se_2O_8]_n^{n+}$ series follows a different assembly logic. Members with $n = 3$–6 can be

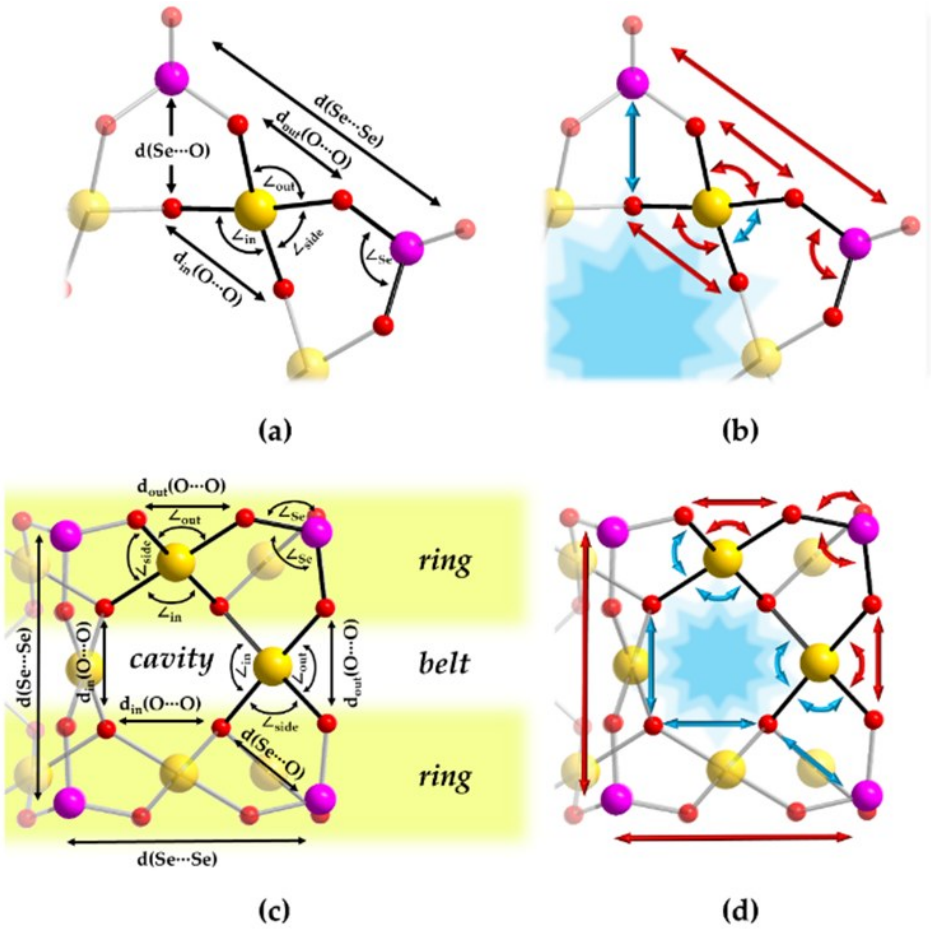


Figure 2: *Geometric descriptors used to analyse strain in the ring-type and cage-type polyoxoaurates. (a) Characteristic distances and angles in a representative ring fragment. (b) Direction of geometric compression/expansion across the ring series. (c) Analogous descriptors for the cage-type architectures, highlighting the outer rim, belt, and oxo cavity. (d) Direction of geometric changes across the cage series.*

viewed as two $\{Au_nSe_nO_{4n}\}$ ring-like fragments bridged by n additional Au^{III} centres, giving trigonal-prismatic, cubic, pentagonal-prismatic, and hexagonal-prismatic cages. The $n = 2$ member is again exceptional: it adopts a compact tetrahedral topology—describable as a Keplerate-like arrangement with an inner $\{O_4\}$ tetrahedron enclosed by an $\{Au_6\}$ shell and an outer tetrahedral set of $\{SeO_3\}$ units, and shows the most strongly distorted Au coordination in the cage series, with O–Au–O angles of 119.6°, 93.1°, and 73.7°.

The cubic cage is close to the square-planar ideal (89.6°, 84.4°, 93.0°; full interatomic distances and angles for the cage series are given in Supporting Information, Table S4), and the pentagonal-prismatic cage remains comparably well balanced. By contrast, the trigonal- and hexagonal-prismatic cages impose progressively larger angular anisotropy. In parallel, the outer O···O rim contracts from 3.119–3.151 Å for $n = 3$ to 2.479–2.547 Å for $n = 6$, whereas the side O···O distances expand from 2.745–2.753 to 3.069–3.090 Å.

The larger cages therefore become flatter in one dimension and thicker in another, analogous to the behaviour seen in the ring family.

3.2 Relative Stability and Electronic Properties

Conformers in which the $\{SeO_3\}$ pyramids point towards the more congested side of the assembly are consistently higher in energy than those discussed above, because they shorten non-bonding O$\cdots$O contacts and thereby increase electrostatic repulsion. Partially flipped, intermediate conformers are likewise disfavoured. The preferred configurations are those that relieve local congestion while retaining the preferred geometry of the $\{AuO_4\}$ units.

The representative frontier orbitals and molecular electrostatic potential maps are shown in Fig. 3. The MEP maps confirm that the most negative regions are centred on terminal or peripheral oxygen atoms. In the ring structures these regions are distributed along the oxo belt; in the cages they are concentrated on the outer shell. The most accessible sites for interaction with cationic species therefore lie on the oxygen-rich periphery rather than near the gold centres. Hirshfeld charge analysis (Table S5) corroborates this picture quantitatively: Au carries a positive charge of about $+0.41$ to $+0.43$ in the ring family and about $+0.59$ to $+0.63$ in the cage family, while Se is also positively charged ($+0.47$ to $+0.77$) and the oxygen atoms bear the negative charge (-0.29 to -0.47). The formal oxidation state of Au is $+3$ throughout, dictated by the closed-shell electron count and cluster stoichiometry; the much smaller Hirshfeld values reflect substantial covalency in the Au–O bonding, as is typical for this partitioning scheme applied to transition metals, and should not be read as a reduced effective oxidation state. The range of Au charges is narrow within each family, indicating that the differing overall charge of the clusters ($n-$ for the rings, $n+$ for the cages) is accommodated mainly by the oxo/selenite scaffold rather than by variable Au oxidation states.

The frontier-orbital data confirm that both families are electronically robust across the full $n = 2$–6 range. For the anionic ring series the HOMO–LUMO gaps follow the order $n = 3$ (3.7 eV) $> n = 4$ (3.6 eV) $> n = 5$ (3.5 eV) $> n = 6$ (3.3 eV) $> n = 2$ (3.2 eV), while for the cationic cage series the order is $n = 4$ (3.9 eV) $> n = 5$ (3.8 eV) $> n = 3$ (3.7 eV) $> n = 6$ (3.5 eV) $> n = 2$ (3.2 eV) (see Supporting Information, Table S6). The cage orbitals are overall lower in energy because the cationic scaffold binds electrons more strongly, but both families display similarly large gaps. A gap of 3.2–3.9 eV places these clusters in the same range as many stable, wide-gap metal oxides; the modest 0.7 eV variation across the series reflects differences in Au–O covalency and local strain rather than a fundamental change in electronic character. The smaller gaps of the dimers correlate with their more distorted geometries and point to a slightly higher chemical reactivity for these compact, strained assemblies. Global reactivity descriptors derived from the frontier-orbital energies by Koopmans' theorem (Table S7)[31–33] show that, in both families, the dimers are consistently the softest and most electrophilic members, in line with their comparatively high energy and distorted local geometry. Among the larger, energetically preferred members, hardness and electrophilicity do not track bonding-energy stability exactly: the trimer is the hardest and least electrophilic ring (rather than the energetically preferred tetramer), and the cubic tetramer is the hardest and least electrophilic

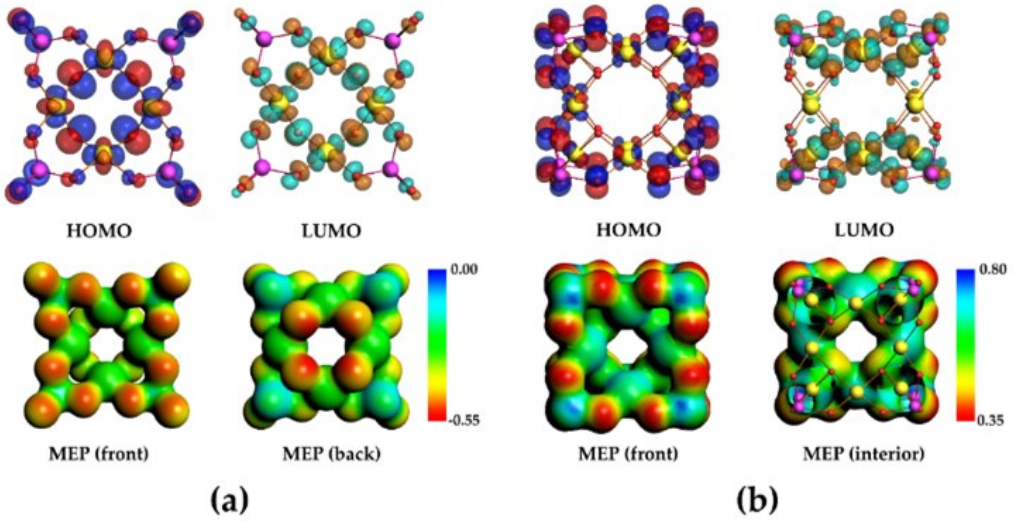


Figure 3: *Frontier orbitals and molecular electrostatic potentials for representative members of the two families: (a) ring-type $[AuSeO_4]_4^{4-}$; (b) cage-type $[Au_3Se_2O_8]_4^{4+}$. Colour code: Au = yellow, Se = violet, O = red spheres. HOMO = red/blue lobes. LUMO = cyan/orange lobes. Red regions in the MEP maps denote the most nucleophilic oxygen-rich sites.*

cage (rather than the energetically preferred pentagonal prism). This indicates that, beyond the clearly destabilised dimers, frontier-orbital hardness and bonding-energy stability are governed by related but not identical aspects of the Au–O framework. The cationic cage family is also markedly more electrophilic than the anionic rings across the whole series ($\omega \approx 14$–18 eV versus 7–10 eV, Table S7), consistent with earlier reports that related compact Au-rich oxo-clusters of this type behave as strong oxidants in solution[5]; a sizeable HOMO–LUMO gap therefore does not preclude these cages from remaining comparatively susceptible to reduction by suitable external reductants.

The HOMO is dominated by O-centred contributions with a subordinate Au component, whereas the LUMO has substantial Au and O character. For the representative tetrameric ring, the HOMO contains approximately 68% O, 21% Au, and 8% Se, while the LUMO contains approximately 54% O and 46% Au (full atomic orbital contributions for all ring members are given in Supporting Information, Table S8). For the cubic cage, the HOMO is even more oxygen-rich, whereas the LUMO is shared almost equally between Au and O, with a modest Se contribution (Supporting Information, Table S9). These orbital compositions are consistent with closed-shell Au(III)-oxo clusters in which the frontier electronic structure is governed mainly by the Au–O framework.

The energetic trends are summarised in Fig. 4. When bonding energies are normalised per repeating unit, the ring series follows the order $n = 4 > 5 > 6 \approx 3 \gg 2$, whereas the cage series follows $n = 5 > 4 > 6 > 3 > 2$. The energetic separation between the most stable members is small: in the ring family the tetramer lies only 10, 23, and 22 kJ mol^{-1} per repeating unit below the pentamer, trimer, and hexamer, respectively, while the dimer is 184 kJ mol^{-1} per repeating unit higher. In the cage family the pentagonal prism is only 4 kJ mol^{-1} per repeating unit below the cubic tetramer, and 34, 103, and 370 kJ mol^{-1}

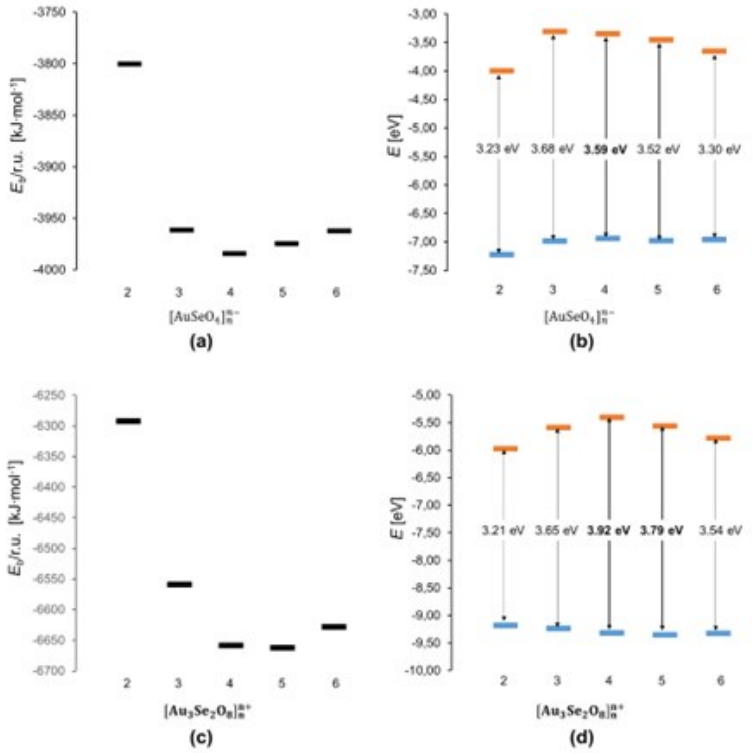


Figure 4: *Energy trends across the two polyoxoaurate families: (a) bonding energy per repeating unit for* $[AuSeO_4]_n^{n-}$*; (b) frontier-orbital energies and HOMO–LUMO gaps for* $[AuSeO_4]_n^{n-}$*; (c) bonding energy per repeating unit for* $[Au_3Se_2O_8]_n^{n+}$*; (d) frontier-orbital energies and HOMO–LUMO gaps for* $[Au_3Se_2O_8]_n^{n+}$*;* $n = 2$–6.

per repeating unit below the hexamer, trimer, and dimer, respectively. All values above are normalised per repeating unit so that clusters of different nuclearity can be compared directly. The pentagonal-prismatic cage is therefore the lowest-energy member on a per-unit basis, with the cubic cage only marginally higher. Both minima coincide with the nuclearities that best preserve square-planar Au coordination. The ring dimer is destabilised by edge-sharing and the short Au$\cdots$Au contact, while the tetrahedral cage dimer is destabilised by the strongly compressed coordination geometry imposed by its compact topology (Table 1). These trends show that the same $\{AuO_4\}$ and $\{SeO_3\}$ building units can produce either anionic rings or cationic cages, but that only selected nuclearities avoid the geometric penalty of assembly. The preferred products are those topologies that best accommodate the local demands of the constituent building blocks, providing a chemically grounded basis for rationalising the experimentally observed members of both series and for assessing candidate polyoxoaurate targets not yet isolated. The predictive value of this strain-based picture extends to the broader design of polyoxometalate-based materials, where local coordination geometry can be used as a pre-synthetic filter alongside symmetry and magic-number arguments.

4 Conclusions

The stability of polyoxoselenitoaurate assemblies is governed primarily by geometric strain in the $\{AuO_4\}$ square-planar and $\{SeO_3\}$ trigonal-pyramidal units. In the ring-type $[AuSeO_4]_n^{n-}$ family, the tetramer $[AuSeO_4]_4^{4-}$ provides the best compromise between ring closure and local square-planar coordination, whereas smaller and larger rings are more distorted. The dimer represents a limiting case, with an edge-sharing topology and a short Au$\cdots$Au contact indicative of incipient aurophilic interaction. In the cage-type $[Au_3Se_2O_8]_n^{n+}$ family, the pentamer $[Au_3Se_2O_8]_5^{5+}$ is the lowest-energy member per repeating unit, with the cubic tetramer $[Au_3Se_2O_8]_4^{4+}$ close behind. The tetrahedral dimer is the most strained cage member, mirroring the geometric argument that applies to the ring dimer.

These findings qualify broader magic-number arguments in polyoxo-noble-metalate chemistry. Work on polyoxopalladates and giant molecular rings has shown that building-block and symmetry relationships can suggest many possible nuclearities [52, 53]. The present results show that such proposals must also satisfy the local coordination geometry of the building units. In the polyoxoaurate systems studied here, several formally reasonable assemblies become less plausible because they distort the square-planar Au(III) environments or introduce short non-bonding O$\cdots$O contacts. In both families, the most stable members coincide with the least distorted local Au environments, confirming that strain minimisation is a useful predictive criterion for cluster formation. The frontier-orbital and Hirshfeld analyses further show that the electronic structure remains robust across the series, with Au retaining its formal $+3$ oxidation state throughout despite a substantially smaller Hirshfeld partial charge, and the oxo/selenite scaffold accommodating the overall cluster charge. The calculations rationalise the experimentally observed nuclearities and provide a geometry-based framework for assessing new polyoxoaurate and related polyoxometalate architectures. Because the strain criterion is independent of the specific metal or linker, it should be transferable to other noble-metal-containing polyoxometalates and to the targeted synthesis of POM-based functional materials.

Author Contributions

A.K. conceived the study, developed the methodology and software, performed the calculations and formal analysis, and wrote and revised the manuscript.

Data Availability

The optimised geometries reported in this work are provided in the Supporting Information. The POMAssembler code used to generate the initial polyoxoaurate structures is freely available under the MIT licence via Zenodo, https://doi.org/10.5281/zenodo.21250229 [17].

Acknowledgements

A.K. thanks the Field of Expertise – Advanced Materials Science of Graz University of Technology for Competitive Start-up Funding support (AF22-635-1).

Declaration of Competing Interest

The author declares no competing interests.

Abbreviations

POMs	Polyoxometalates
TZP	Triple-zeta plus polarisation (basis set)
ZORA	Zero-order regular approximation
COSMO	Conductor-like screening model
BP86	Becke–Perdew 1986 exchange–correlation functional
B3LYP	Becke three-parameter Lee–Yang–Parr hybrid functional
DFT	Density functional theory
GGA	Generalised gradient approximation
HOMO	Highest occupied molecular orbital
LUMO	Lowest unoccupied molecular orbital
MEP	Molecular electrostatic potential

Declaration of Generative AI and AI-Assisted Technologies in the Manuscript Preparation Process

During the preparation of this work, the author used ChatGPT (OpenAI) for text polishing. The author reviewed and edited the output as needed and takes full responsibility for the content of the published article.

A Tables

Table S1: *Calculated characteristic bond lengths for $[Au_3Se_2O_8]_n^{n+}$ and $[AuSeO_4]_n^{n-}$. Data obtained at the BP86/TZP/ZORA-scalar/COSMO-water level.*

Model	**Se–O_b [Å]**	**Au–O [Å]**	**Model**	**Se–O_t [Å]**	**Se–O_b [Å]**	**Au–O [Å]**
$[Au_3Se_2O_8]_2^{2+}$	1.860	2.018; 2.051	$[AuSeO_4]_2^{2-}$	1.677	1.871	2.097; 2.098
$[Au_3Se_2O_8]_3^{3+}$	1.790; 1.792	1.997–2.034	$[AuSeO_4]_3^{3-}$	1.681	1.843	2.022; 2.055
$[Au_3Se_2O_8]_4^{4+}$	1.772	2.018; 2.024	$[AuSeO_4]_4^{4-}$	1.680	1.816	2.010; 2.053
$[Au_3Se_2O_8]_5^{5+}$	1.758; 1.759	2.015–2.048	$[AuSeO_4]_5^{5-}$	1.677	1.802	2.016; 2.057
$[Au_3Se_2O_8]_6^{6+}$	1.749; 1.752	2.019–2.082	$[AuSeO_4]_6^{6-}$	1.677	1.798	2.023; 2.056

Table S2: *Calculated angles for $[AuSeO_4]_n^{n-}$. Data obtained at the BP86/TZP/ZORA-scalar/COSMO-water level. ∠planes = dihedral between adjacent $\{AuO_4\}$ mean planes; out/in/o·in = O–Au–O descriptors defined in the main text; $\angle O_b$–Se–O_b = bridging O–Se–O angle.*

Model	∠planes (°)	$\angle_{out}$O–Au–O (°)	$\angle_{in}$O–Au–O (°)	$\angle_{o/in}$O–Au–O (°)	$\angle O_b$–Se–O_b (°)
$[AuSeO_4]_2^{2-}$	—	97.0	78.9	84.6	109.7
$[AuSeO_4]_3^{3-}$	127.8	95.1	93.6	85.4	103.3
$[AuSeO_4]_4^{4-}$	132.5	87.2	93.3	89.7	101.1
$[AuSeO_4]_5^{5-}$	137.9	81.2	90.3	94.0	99.3
$[AuSeO_4]_6^{6-}$	150.5	80.6	85.6	96.7	98.7

Table S3: *Calculated interatomic distances for $[AuSeO_4]_n^{n-}$. Data obtained at the BP86/TZP/ZORA-scalar/COSMO-water level.*

Model	d(Se···μ_2-O) (Å)	d_{Se}(Se···Se) (Å)	d_{Se}(O···O) (Å)	d_{out}(O···O) (Å)	d_{in}(O···O) (Å)	d_{side}(O···O) (Å)
$[AuSeO_4]_2^{2-}$	2.648	5.294	3.072	3.094	2.665	2.824
$[AuSeO_4]_3^{3-}$	2.628	6.322	2.896	3.038	2.947	2.768
$[AuSeO_4]_4^{4-}$	2.789	6.223	2.804	2.832	2.923	2.865
$[AuSeO_4]_5^{5-}$	3.013	6.031	2.746	2.677	2.858	2.980
$[AuSeO_4]_6^{6-}$	3.131	5.814	2.728	2.661	2.741	3.048

Table S4: *Calculated interatomic distances and angles for $[Au_3Se_2O_8]_n^{n+}$. Data obtained at the BP86/TZP/ZORA-scalar/COSMO-water level. Labels r and b denote ring and belt sites, respectively.*

Model	d(Se···O) (Å)	d(Se···Se) (Å)	d_{out} (Å)	d_{in} (Å)	d_{side} (Å)	∠(O–Se–O) (°)	d(O···O)$_{Se}$ (Å)
$[Au_3Se_2O_8]_2^{2+}$	2.125	6.398	3.546	2.929	2.424	113.7	3.115
$[Au_3Se_2O_8]_3^{3+}$	2.824	6.380 r 6.461 b	3.151 r 3.119 b	2.712 r 2.694 b	2.753 r 2.745 b	108.1 r 108.8 b	2.898 r 2.912 b
$[Au_3Se_2O_8]_4^{4+}$	3.096	6.295	2.844	2.720	2.932	106.7	2.843
$[Au_3Se_2O_8]_5^{5+}$	3.263	6.067 r 6.152 b	2.622 r 2.660 b	2.778 r 2.792 b	3.035 r 3.017 b	104.3 r 105.7 b	2.776 r 2.804 b
$[Au_3Se_2O_8]_6^{6+}$	3.358	5.860 r 6.044 b	2.479 r 2.547 b	2.955 r 2.853 b	3.090 r 3.069 b	102.1 r 105.3 b	2.720 r 2.784 b

Table S5: *Hirshfeld atomic charges (average and, where inequivalent, range) for* $[Au_3Se_2O_8]_n^{n+}$ *and* $[AuSeO_4]_n^{n-}$. *Positive values indicate electron depletion relative to the neutral atom. Data obtained at the B3LYP/TZP/ZORA-scalar/COSMO-water level.*

Model	Au charge	Se charge	O charge
$[AuSeO_4]_n^{n-}$			
$n=2$	+0.408	+0.475	−0.471 (−0.543 to −0.442)
$n=3$	+0.419	+0.470	−0.472 (−0.560 to −0.438)
$n=4$	+0.430	+0.466	−0.474 (−0.563 to −0.430)
$n=5$	+0.430	+0.470	−0.475 (−0.557 to −0.427)
$n=6$	+0.424	+0.474	−0.475 (−0.552 to −0.421)
$[Au_3Se_2O_8]_n^{n+}$			
$n=2$	+0.618	+0.727	−0.289 (−0.298 to −0.262)
$n=3$	+0.629 (+0.619 to +0.647)	+0.739	−0.295 (−0.313 to −0.290)
$n=4$	+0.613	+0.752	−0.293 (−0.306 to −0.288)
$n=5$	+0.600 (+0.581 to +0.609)	+0.763	−0.291 (−0.304 to −0.285)
$n=6$	+0.592 (+0.563 to +0.606)	+0.769	−0.289 (−0.305 to −0.282)

Table S6: *Frontier-orbital energies, HOMO–LUMO gaps, and bonding energies per repeating unit for $[Au_3Se_2O_8]_n^{n+}$ and $[AuSeO_4]_n^{n-}$. E_{HOMO}: energy of the highest occupied molecular orbital; E_{LUMO}: energy of the lowest unoccupied molecular orbital; ΔE_{HL}: HOMO–LUMO gap; $E_{b/r.u.}$: total bonding energy (from ADF output) divided by the number of repeating units n. Data obtained at the B3LYP/TZP/ZORA-scalar/COSMO-water level. The ring and cage families have different absolute frontier-orbital energies because they carry opposite overall charges, but the gap trends are similar.*

Model	E_{HOMO} [eV]	E_{LUMO} [eV]	ΔE_{HL} [eV]	$E_{\mathrm{b/r.u.}}$ [kJ mol^{-1}]
$[Au_3Se_2O_8]_n^{n+}$				
$n = 2$	−9.16	−5.96	3.21	−6290.69
$n = 3$	−9.22	−5.57	3.65	−6557.48
$n = 4$	−9.30	−5.39	3.92	−6656.59
$n = 5$	−9.33	−5.55	3.79	−6660.65
$n = 6$	−9.30	−5.77	3.54	−6626.87
$[AuSeO_4]_n^{n-}$				
$n = 2$	−7.21	−4.02	3.19	−3799.30
$n = 3$	−6.96	−3.28	3.68	−3960.68
$n = 4$	−6.91	−3.32	3.59	−3983.47
$n = 5$	−6.95	−3.43	3.52	−3973.66
$n = 6$	−6.93	−3.63	3.30	−3961.15

Table S7: *Global reactivity descriptors derived from the B3LYP frontier-orbital energies by Koopmans' theorem: chemical hardness $\eta = (E_{LUMO} - E_{HOMO})/2$, softness $S = 1/\eta$, chemical potential $\mu = (E_{HOMO} + E_{LUMO})/2$, electronegativity $\chi = -\mu$, and electrophilicity index $\omega = \mu^2/(2\eta)$. All values are in eV.*

Model	η	S	μ	χ	ω
$[AuSeO_4]_n^{n-}$					
$n = 2$	1.60	0.63	−5.62	5.62	9.88
$n = 3$	1.84	0.54	−5.12	5.12	7.12
$n = 4$	1.80	0.56	−5.12	5.12	7.29
$n = 5$	1.76	0.57	−5.19	5.19	7.65
$n = 6$	1.65	0.61	−5.28	5.28	8.45
$[Au_3Se_2O_8]_n^{n+}$					
$n = 2$	1.61	0.62	−7.56	7.56	17.81
$n = 3$	1.83	0.55	−7.40	7.40	14.98
$n = 4$	1.96	0.51	−7.35	7.35	13.76
$n = 5$	1.90	0.53	−7.44	7.44	14.61
$n = 6$	1.78	0.57	−7.54	7.54	16.04

Table S8: *Atomic orbital contributions to the HOMO and LUMO for $[AuSeO_4]_n^{n-}$. Δ(LUMO−HOMO) is the difference in percentage contribution. Data obtained at the B3LYP/TZP/ZORA-scalar/COSMO-water level.*

Model	**State**	**Au [%]**	**O [%]**	**Se [%]**
$[AuSeO_4]_2^{2-}$	HOMO	15.95	68.11	13.96
	LUMO	40.45	55.63	1.83
	Δ(LUMO−HOMO)	+24.50	−12.48	−12.13
$[AuSeO_4]_3^{3-}$	HOMO	19.29	59.51	12.05
	LUMO	40.37	52.27	1.90
	Δ(LUMO−HOMO)	+21.08	−7.24	−10.15
$[AuSeO_4]_4^{4-}$	HOMO	20.77	67.87	7.99
	LUMO	43.54	54.04	2.49
	Δ(LUMO−HOMO)	+22.77	−13.83	−5.50
$[AuSeO_4]_5^{5-}$	HOMO	18.49	74.57	1.37
	LUMO	42.96	53.28	2.00
	Δ(LUMO−HOMO)	+24.47	−21.29	+0.63
$[AuSeO_4]_6^{6-}$	HOMO	14.31	81.89	3.02
	LUMO	42.93	55.63	1.54
	Δ(LUMO−HOMO)	+28.62	−26.26	−1.48

Table S9: *Atomic orbital contributions to the HOMO and LUMO for* $[Au_3Se_2O_8]_n^{n+}$. *Δ(LUMO−HOMO) is the difference in percentage contribution. Data obtained at the B3LYP/TZP/ZORA-scalar/COSMO-water level.*

Model	**State**	**Au [%]**	**O [%]**	**Se [%]**
$[Au_3Se_2O_8]_2^{2+}$	HOMO	14.21	85.76	0.00
	LUMO	41.38	50.10	6.33
	Δ(LUMO−HOMO)	+27.17	−35.66	+6.33
$[Au_3Se_2O_8]_3^{3+}$	HOMO	17.77	77.31	1.14
	LUMO	40.70	47.54	7.80
	Δ(LUMO−HOMO)	+22.93	−29.77	+6.66
$[Au_3Se_2O_8]_4^{4+}$	HOMO	14.40	84.83	0.00
	LUMO	44.83	43.79	8.34
	Δ(LUMO−HOMO)	+30.43	−41.04	+8.34
$[Au_3Se_2O_8]_5^{5+}$	HOMO	19.76	77.04	0.00
	LUMO	43.42	44.62	5.18
	Δ(LUMO−HOMO)	+23.66	−32.42	+5.18
$[Au_3Se_2O_8]_6^{6+}$	HOMO	19.10	76.11	0.00
	LUMO	43.06	44.13	4.86
	Δ(LUMO−HOMO)	+23.96	−31.98	+4.86

B POMAssembler workflow and comparison with conventional builders

POMAssembler is a topology-driven, rigid-block construction tool that extends an earlier assembler for metal–organic polyhedra [22]. It was written for the present study and released under the MIT licence via Zenodo, https://doi.org/10.5281/zenodo.21250229 [17]. Its purpose is to generate chemically reasonable starting geometries for a family of related polyoxometalate architectures without requiring manually assembled coordinates for each nuclearity.

Conventional model builders typically fall into two classes: (i) fragment-based assemblers that place and connect pre-optimised molecular fragments atom-by-atom, and (ii) crystal-engineering toolkits that build periodic lattices from symmetry operations. POMAssembler differs from both in that it works with rigid polyhedral building blocks and connector sites. A target topology is specified by a graph of shared metal positions; each block is then fitted to its assigned connector sites by a rigid transformation (axis alignment for two-connector blocks, Kabsch alignment with an outward-direction constraint for three-connector blocks).

The treatment of shared junctions is where POMAssembler departs from the earlier MOP assembler [22]. In that tool, the metal building blocks carry no oxygen atoms at their connection points: all bridging atoms are supplied exclusively by the organic (carboxylate) linker blocks, so each junction is populated from a single, unambiguous source. Here the repeating building unit is itself a metal-oxo block ($\{AuO_4\}$, $\{Au_3SeO_3\}$) that inherently carries oxygen atoms at its own connector positions. When two such blocks are joined at a shared metal site, each block therefore contributes its own copy of what should be a single bridging oxygen atom, so partial, overlapping oxygen atoms accumulate at that position. POMAssembler adds a dedicated sanitisation step – not required by the earlier MOP assembler – that identifies coincident metal atoms and these duplicated, fractional oxygen atoms at each junction and merges them into a single atom before the resulting coordinates are passed to quantum-chemical optimisation. This block-level approach makes it easy to preserve the local coordination geometry of the building units while scanning nuclearity and topology, which is the central requirement for the strain-analysis presented in the main text.

The rigid-block strategy is conceptually related to the polyhedral representations used in POM topology software [34, 35], but it is applied here to generate full three-dimensional coordinates for finite molecular clusters rather than to classify idealised frameworks.

C Notes on the electronic-structure analysis

The Hirshfeld charges reported in Table S5 were taken directly from the B3LYP single-point output. Hirshfeld partitioning is a widely used scheme for assigning molecular electron density to atoms and has been employed in analogous DFT studies of optical and electronic materials [1, 2, 29, 36–38, 49, 50]. Because the same level of theory and the same integration grid are used for all members of each series, the relative charge trends

are robust, even though absolute atomic charges are method-dependent.

The global reactivity descriptors in Table S7 were obtained from the HOMO and LUMO energies by Koopmans' theorem ($I \approx -E_{\mathrm{HOMO}}$, $A \approx -E_{\mathrm{LUMO}}$) following the standard conceptual-DFT definitions [31–33]. They are reported for comparative purposes across the series; their absolute values depend on the functional and should not be compared directly with experiment without calibration.

D Optimised Geometries

All geometries were optimised at the BP86/ZORA-scalar/TZP/COSMO-water level (closed shell). Coordinates are given in Angstroms (Cartesian).

Ring-type family: $[\mathrm{AuSeO_4}]_n^{n-}$

$[\mathrm{AuSeO_4}]_2^{2-}$

O	3.12841132	0.00000000	1.90827706
O	-1.57209504	1.52976776	0.36370593
O	1.57209504	1.52976776	0.36370593
Se	2.64714993	0.00000000	0.30147910
O	1.33264585	0.00000000	-1.99740331
O	-1.33264585	0.00000000	-1.99740331
O	-1.57209504	-1.52976776	0.36370593
Au	0.00000000	-1.27650713	-1.00226452
O	-3.12841132	0.00000000	1.90827706
Se	-2.64714993	0.00000000	0.30147910
O	1.57209504	-1.52976776	0.36370593
Au	0.00000000	1.27650713	-1.00226452

$[\mathrm{AuSeO_4}]_3^{3-}$

O	-2.30059534	-3.98474801	1.42842860
O	-0.04284551	2.96425839	0.46793482
O	2.58854583	1.44502389	0.46793482
O	1.70164486	0.00000000	-1.72015942
O	-0.85082243	-1.47366768	-1.72015942
O	-0.85082243	1.47366768	-1.72015942
O	-2.54570031	1.51923450	0.46793482
O	-2.54570031	-1.51923450	0.46793482
O	-2.30059534	3.98474801	1.42842860
Se	-1.82512882	3.16121585	0.04261040
Au	0.88232924	-1.52823907	-0.68032188
Au	0.88232924	1.52823907	-0.68032188
Au	-1.76465848	0.00000000	-0.68032188
O	4.60119068	0.00000000	1.42842860
O	-0.04284551	-2.96425839	0.46793482
O	2.58854583	-1.44502389	0.46793482
Se	3.65025764	0.00000000	0.04261040
Se	-1.82512882	-3.16121585	0.04261040

$[\mathrm{AuSeO_4}]_4^{4-}$

Se	3.11158473	-3.11158473	0.03271072
O	-3.39822778	-1.41584070	-0.54942819
O	-3.39822778	1.41584070	-0.54942819
Se	3.11158473	3.11158473	0.03271072
O	3.39822778	-1.41584070	-0.54942819
Au	0.00000000	-2.35980209	0.51379965
O	3.39822778	1.41584070	-0.54942819
Au	0.00000000	2.35980209	0.51379965
O	3.94047982	-3.94047982	-1.17059599
O	1.41584070	-3.39822778	-0.54942819
O	-1.41584070	-3.39822778	-0.54942819
Se	-3.11158473	-3.11158473	0.03271072
O	-1.46170678	1.46170678	1.56131451
O	-1.41584070	3.39822778	-0.54942819
O	3.94047982	3.94047982	-1.17059599
O	1.41584070	3.39822778	-0.54942819
O	-3.94047982	3.94047982	-1.17059599
O	-3.94047982	-3.94047982	-1.17059599
O	1.46170678	1.46170678	1.56131451
O	-1.46170678	-1.46170678	1.56131451
Au	-2.35980209	0.00000000	0.51379965
O	1.46170678	-1.46170678	1.56131451
Au	2.35980209	0.00000000	0.51379965
Se	-3.11158473	3.11158473	0.03271072

$[\mathrm{AuSeO_4}]_5^{5-}$

O	-1.96715993	-1.42922552	-1.41512539
O	-1.96715993	1.42922552	-1.41512539
Se	-4.15082338	-3.01574989	-0.07562711
Au	-2.96050226	0.00000000	-0.39697677
Au	-0.91484535	-2.81560520	-0.39697677
Se	-4.15082338	3.01574989	-0.07562711
Au	-0.91484535	2.81560520	-0.39697677
O	0.75138856	-2.31253547	-1.41512539
O	-5.18414889	-3.76650481	1.01083355
O	-4.17773314	-1.33836588	0.58142162
O	-2.56385197	-3.55968275	0.58142162
O	-4.17773314	1.33836588	0.58142162
O	-0.01812878	-4.38683835	0.58142162
O	0.75138856	2.31253547	-1.41512539
O	-2.56385197	3.55968275	0.58142162
O	-5.18414889	3.76650481	1.01083355
O	-0.01812878	4.38683835	0.58142162
Se	1.58547378	-4.87958582	-0.07562711
Au	2.39509707	-1.74013971	-0.39697677
Se	1.58547378	4.87958582	-0.07562711
Au	2.39509707	1.74013971	-0.39697677
O	2.43154393	0.00000000	-1.41512539
O	1.98016900	-6.09433280	1.01083355
O	2.59318581	-3.53837081	0.58142162
O	4.16652926	-1.37284932	0.58142162
O	1.98016900	6.09433280	1.01083355
O	2.59318581	3.53837081	0.58142162
O	4.16652926	1.37284932	0.58142162
Se	5.13070039	0.00000000	-0.07562711
O	6.40796096	0.00000000	1.01083355

$[\mathrm{AuSeO_4}]_6^{6-}$

O	2.37970000	1.37392000	-0.97288000

O	2.37970000	-1.37392000	-0.97288000
Se	5.03506000	2.90699000	-0.33677000
Au	3.62621000	-0.00000000	-0.16684000
Au	-1.81310000	3.14039000	-0.16684000
Se	5.03506000	-2.90699000	-0.33677000
Au	1.81310000	-3.14039000	-0.16684000
O	-2.37970000	1.37392000	-0.97288000
O	6.33103000	3.65522000	0.42119000
O	5.03201000	1.33051000	0.52765000
O	3.66826000	3.69259000	0.52765000
O	5.03201000	-1.33051000	0.52765000
O	-3.66826000	3.69259000	0.52765000
O	-0.00000000	-2.74784000	-0.97288000
O	3.66826000	-3.69259000	0.52765000
O	6.33103000	-3.65522000	0.42119000
O	1.36375000	-5.02310000	0.52765000
Se	-5.03506000	2.90699000	-0.33677000
Au	-3.62621000	0.00000000	-0.16684000
Se	-0.00000000	-5.81398000	-0.33677000
Au	-1.81310000	-3.14039000	-0.16684000
O	-2.37970000	-1.37392000	-0.97288000
O	-6.33103000	3.65522000	0.42119000
O	-5.03201000	1.33051000	0.52765000
O	-5.03201000	-1.33051000	0.52765000
O	-0.00000000	-7.31044000	0.42119000
O	-1.36375000	-5.02310000	0.52765000
O	-3.66826000	-3.69259000	0.52765000
Se	-5.03506000	-2.90699000	-0.33677000
O	-6.33103000	-3.65522000	0.42119000
Au	1.81310000	3.14039000	-0.16684000
O	0.00000000	2.74784000	-0.97288000
Se	0.00000000	5.81398000	-0.33677000
O	0.00000000	7.31044000	0.42119000
O	-1.36375000	5.02310000	0.52765000
O	1.36375000	5.02310000	0.52765000

Cage-type family: $[Au_3Se_2O_8]_n^{n+}$

$[Au_3Se_2O_8]_2^{2+}$

Au	2.41064678	0.00000000	-0.00000000
Au	0.00000000	0.00000000	-2.41064678
O	1.25135809	3.42973299	-1.25135809
Se	2.25321661	2.25321661	-2.25321661
O	1.02653971	1.02653971	-1.02653971
Au	0.00000000	2.41064678	-0.00000000
O	1.25135809	1.25135809	-3.42973299
O	3.42973299	1.25135809	-1.25135809
Au	-2.41064678	0.00000000	-0.00000000
Au	0.00000000	-2.41064678	-0.00000000
O	-1.02653971	1.02653971	1.02653971
O	-1.25135809	-3.42973299	-1.25135809
O	1.02653971	-1.02653971	1.02653971
Au	0.00000000	0.00000000	2.41064678
O	-1.02653971	-1.02653971	-1.02653971
O	1.25135809	-3.42973299	1.25135809
O	1.25135809	-1.25135809	3.42973299
Se	2.25321661	-2.25321661	2.25321661
O	3.42973299	-1.25135809	1.25135809
O	-1.25135809	1.25135809	3.42973299
Se	-2.25321661	2.25321661	2.25321661
O	-3.42973299	1.25135809	1.25135809
O	-1.25135809	3.42973299	1.25135809
O	-3.42973299	-1.25135809	-1.25135809
Se	-2.25321661	-2.25321661	-2.25321661
O	-1.25135809	-1.25135809	-3.42973299

$[Au_3Se_2O_8]_3^{3+}$

O	2.14956776	-3.72315989	1.56140963
O	-2.64203237	1.43290569	3.42944170
O	0.08008404	3.00452034	3.42944170
O	0.78132981	1.35330225	1.34058367
O	0.78132981	-1.35330225	1.34058367
O	-1.56265845	0.00000000	1.34058367
O	-2.64203237	-1.43290569	3.42944170
O	0.08008404	-3.00452034	3.42944170
O	-4.29913434	0.00000000	1.56140963
Se	-3.66962043	0.00000000	3.22140096
Au	1.81684846	0.00000000	2.39610323
Au	-0.90842365	1.57343659	2.39610323
Au	-0.90842365	-1.57343659	2.39610323
O	2.14956776	3.72315989	1.56140963
O	2.56194950	-1.57161465	3.42944170
O	2.56194950	1.57161465	3.42944170
Se	1.83481080	3.17798485	3.22140096
Se	1.83481080	-3.17798485	3.22140096
O	-4.29913434	0.00000000	-1.56140963
O	2.56194950	-1.57161465	-3.42944170
O	2.56194950	1.57161465	-3.42944170
O	0.78132981	1.35330225	-1.34058367
O	-1.56265845	0.00000000	-1.34058367
O	0.78132981	-1.35330225	-1.34058367
O	0.08008404	-3.00452034	-3.42944170
O	-2.64203237	-1.43290569	-3.42944170
O	2.14956776	-3.72315989	-1.56140963
Se	1.83481080	-3.17798485	-3.22140096
Au	-0.90842365	1.57343659	-2.39610323
Au	1.81684846	0.00000000	-2.39610323
Au	-0.90842365	-1.57343659	-2.39610323
O	2.14956776	3.72315989	-1.56140963
O	-2.64203237	1.43290569	-3.42944170
O	0.08008404	3.00452034	-3.42944170
Se	1.83481080	3.17798485	-3.22140096
Se	-3.66962043	0.00000000	-3.22140096
Au	1.51234747	2.61946199	-0.00000000
Au	1.51234747	-2.61946199	-0.00000000
Au	-3.02469378	0.00000000	-0.00000000

$[Au_3Se_2O_8]_4^{4+}$

Au	-0.00000000	-2.41960568	2.41960568
O	1.35984864	-1.35984864	1.35984864
O	-1.35984864	-1.35984864	1.35984864
O	-1.42177149	-3.43239756	3.43239756
O	1.42177149	-3.43239756	3.43239756
Au	2.41960568	-0.00000000	2.41960568
Au	2.41960568	-2.41960568	0.00000000
O	-3.43239756	-1.42177149	-3.43239756
Au	-2.41960568	-0.00000000	2.41960568
Au	-2.41960568	-2.41960568	0.00000000
Se	-3.14752890	-3.14752890	3.14752890
Se	3.14752890	-3.14752890	3.14752890
O	1.35984864	1.35984864	1.35984864
O	3.43239756	-1.42177149	3.43239756
O	3.43239756	1.42177149	3.43239756
O	1.35984864	-1.35984864	-1.35984864
O	3.43239756	-3.43239756	1.42177149
O	3.43239756	-3.43239756	-1.42177149
O	1.35984864	1.35984864	-1.35984864
O	-1.35984864	1.35984864	1.35984864
O	-1.35984864	-1.35984864	-1.35984864
O	-1.35984864	1.35984864	-1.35984864
O	-3.43239756	1.42177149	3.43239756
O	-3.43239756	-1.42177149	3.43239756
O	-3.43239756	-3.43239756	-1.42177149
O	-3.43239756	-3.43239756	1.42177149
Au	-0.00000000	2.41960568	2.41960568
Au	2.41960568	2.41960568	0.00000000
Se	3.14752890	3.14752890	3.14752890
Au	-0.00000000	-2.41960568	-2.41960568
Au	2.41960568	-0.00000000	-2.41960568
Se	3.14752890	-3.14752890	-3.14752890
Au	-0.00000000	2.41960568	-2.41960568
Au	-2.41960568	2.41960568	0.00000000
Au	-2.41960568	-0.00000000	-2.41960568
Se	-3.14752890	3.14752890	3.14752890
Se	-3.14752890	-3.14752890	-3.14752890
O	-1.42177149	3.43239756	3.43239756
O	1.42177149	3.43239756	3.43239756
O	3.43239756	3.43239756	1.42177149
O	3.43239756	3.43239756	-1.42177149
Se	-3.14752890	3.14752890	-3.14752890
O	-1.42177149	-3.43239756	-3.43239756
O	1.42177149	-3.43239756	-3.43239756

O	3.43239756	-1.42177149	-3.43239756
O	3.43239756	1.42177149	-3.43239756
Se	3.14752890	3.14752890	-3.14752890
O	-1.42177149	3.43239756	-3.43239756
O	1.42177149	3.43239756	-3.43239756
O	-3.43239756	3.43239756	-1.42177149
O	-3.43239756	3.43239756	1.42177149
O	-3.43239756	1.42177149	-3.43239756

$[Au_3Se_2O_8]_5^{5+}$

Se	-5.16093991	-0.00000000	-3.07602328
O	1.91180949	1.38901103	1.39614026
O	1.91180949	1.38901103	-1.39614026
O	1.91180949	-1.38901103	1.39614026
O	1.91180949	-1.38901103	-1.39614026
O	-0.73024649	-2.24746706	1.39614026
O	-0.73024649	-2.24746706	-1.39614026
O	-2.36312689	-0.00000000	1.39614026
O	-2.36312689	-0.00000000	-1.39614026
O	-0.73024649	2.24746706	1.39614026
O	-0.73024649	2.24746706	-1.39614026
Au	3.00409509	-0.00000000	2.43184893
Au	3.12112404	2.26762948	0.00000000
Au	0.92831631	2.85706438	2.43184893
Au	3.00409509	-0.00000000	-2.43184893
Au	0.92831631	2.85706438	-2.43184893
Au	3.12112404	-2.26762948	0.00000000
Au	0.92831631	-2.85706438	2.43184893
Au	0.92831631	-2.85706438	-2.43184893
Au	-2.43036430	-1.76576289	2.43184893
Au	-1.19216354	-3.66910157	0.00000000
Au	-2.43036430	-1.76576289	-2.43184893
Au	-2.43036430	1.76576289	2.43184893
Au	-3.85792188	-0.00000000	0.00000000
Au	-2.43036430	1.76576289	-2.43184893
Au	-1.19216354	3.66910157	0.00000000
O	4.16573034	1.31109444	3.42761572
O	4.16573034	-1.31109444	3.42761572
O	4.35226956	3.16210906	1.33019180
O	4.35226956	3.16210906	-1.33019180
O	0.04035644	4.36699561	3.42761572
O	2.53420625	3.55669469	3.42761572
O	4.16573034	1.31109444	-3.42761572
O	4.16573034	-1.31109444	-3.42761572
O	0.04035644	4.36699561	-3.42761572
O	2.53420625	3.55669469	-3.42761572
O	4.35226956	-3.16210906	-1.33019180
O	4.35226956	-3.16210906	1.33019180
O	0.04035644	-4.36699561	3.42761572
O	2.53420625	-3.55669469	3.42761572
O	0.04035644	-4.36699561	-3.42761572
O	2.53420625	-3.55669469	-3.42761572
O	-2.59950498	-3.50925264	3.42761572
O	-4.14078893	-1.38785728	3.42761572
O	-1.66241929	-5.11639994	1.33019180
O	-1.66241929	-5.11639994	-1.33019180
O	-2.59950498	-3.50925264	-3.42761572
O	-4.14078893	-1.38785728	-3.42761572
O	-4.14078893	1.38785728	3.42761572
O	-2.59950498	3.50925264	3.42761572
O	-5.37970143	-0.00000000	1.33019180
O	-5.37970143	-0.00000000	-1.33019180
O	-4.14078893	1.38785728	-3.42761572
O	-2.59950498	3.50925264	-3.42761572
O	-1.66241929	5.11639994	1.33019180
O	-1.66241929	5.11639994	-1.33019180
Se	4.17528777	3.03352426	3.07602328
Se	4.17528777	-3.03352426	3.07602328
Se	4.17528777	3.03352426	-3.07602328
Se	-1.59481826	4.90834536	3.07602328
Se	4.17528777	-3.03352426	-3.07602328
Se	-1.59481826	4.90834536	-3.07602328
Se	-1.59481826	-4.90834536	3.07602328
Se	-1.59481826	-4.90834536	-3.07602328
Se	-5.16093991	-0.00000000	3.07602328

$[Au_3Se_2O_8]_6^{6+}$

O	2.51595255	-1.45258588	1.42657207
O	0.00000000	-2.90517176	1.42657207
Se	5.07499156	-2.93004774	3.02177878
Au	1.80751752	-3.13071218	2.43472469
Au	1.80751752	3.13071218	2.43472469
Se	0.00000000	-5.86009548	3.02177878
Au	-1.80751752	-3.13071218	2.43472469
O	0.00000000	2.90517176	1.42657207
O	5.17024814	-2.98504416	1.27337170
O	3.50704654	-3.59536451	3.42074127
O	4.86720027	-1.23950915	3.42074127
O	1.36015373	-4.83487365	3.42074127
O	1.36015373	4.83487365	3.42074127
O	-2.51595255	-1.45258588	1.42657207
O	-1.36015373	-4.83487365	3.42074127
O	0.00000000	-5.97008831	1.27337170
O	-3.50704654	-3.59536451	3.42074127
Se	0.00000000	5.86009548	3.02177878
Au	-1.80751752	3.13071218	2.43472469
Se	-5.07499156	-2.93004774	3.02177878
Au	-3.61503504	0.00000000	2.43472469
O	-2.51595255	1.45258588	1.42657207
O	0.00000000	5.97008831	1.27337170
O	-1.36015373	4.83487365	3.42074127
O	-3.50704654	3.59536451	3.42074127
O	-5.17024814	-2.98504416	1.27337170
O	-4.86720027	-1.23950915	3.42074127
O	-4.86720027	1.23950915	3.42074127
Se	-5.07499156	2.93004774	3.02177878
O	-5.17024814	2.98504416	1.27337170
Au	3.61503504	0.00000000	2.43472469
O	2.51595255	1.45258588	1.42657207
Se	5.07499156	2.93004774	3.02177878
O	5.17024814	2.98504416	1.27337170
O	3.50704654	3.59536451	3.42074127
O	4.86720027	1.23950915	3.42074127
O	2.51595255	1.45258588	-1.42657207
O	0.00000000	2.90517176	-1.42657207
Se	5.07499156	2.93004774	-3.02177878
Au	1.80751752	3.13071218	-2.43472469
Au	1.80751752	-3.13071218	-2.43472469
Se	0.00000000	5.86009548	-3.02177878
Au	-1.80751752	3.13071218	-2.43472469
O	0.00000000	-2.90517176	-1.42657207
O	5.17024814	2.98504416	-1.27337170
O	3.50704654	3.59536451	-3.42074127
O	4.86720027	1.23950915	-3.42074127
O	1.36015373	4.83487365	-3.42074127
O	1.36015373	-4.83487365	-3.42074127
O	-2.51595255	1.45258588	-1.42657207
O	-1.36015373	4.83487365	-3.42074127
O	0.00000000	5.97008831	-1.27337170
O	-3.50704654	3.59536451	-3.42074127
Se	0.00000000	-5.86009548	-3.02177878
Au	-1.80751752	-3.13071218	-2.43472469
Se	-5.07499156	2.93004774	-3.02177878
Au	-3.61503504	0.00000000	-2.43472469
O	-2.51595255	-1.45258588	-1.42657207
O	0.00000000	-5.97008831	-1.27337170
O	-1.36015373	-4.83487365	-3.42074127
O	-3.50704654	-3.59536451	-3.42074127
O	-5.17024814	2.98504416	-1.27337170
O	-4.86720027	1.23950915	-3.42074127
O	-4.86720027	-1.23950915	-3.42074127
Se	-5.07499156	-2.93004774	-3.02177878
O	-5.17024814	-2.98504416	-1.27337170
Au	3.61503504	0.00000000	-2.43472469
O	2.51595255	-1.45258588	-1.42657207
Se	5.07499156	-2.93004774	-3.02177878
O	5.17024814	-2.98504416	-1.27337170
O	3.50704654	-3.59536451	-3.42074127
O	4.86720027	-1.23950915	-3.42074127
Au	3.80475572	-2.19667674	-0.00000000
Au	3.80475572	2.19667674	-0.00000000
Au	0.00000000	4.39335347	-0.00000000
Au	-3.80475572	2.19667674	-0.00000000
Au	-3.80475572	-2.19667674	-0.00000000
Au	0.00000000	-4.39335347	-0.00000000

References

[1] S. Akshay Kalyan, S. Elangovan, R. Karthick, N. Kanagathara, M. K. Marchewka, and J. Janczak. Synthesis, XRD, spectral, photoluminescence, optical, electrical conductivity, and dielectric studies on melamine–melaminium 2-acetyl benzoate dihydrate. *J. Mater. Sci. Mater. Electron.*, 35:2100, 2024. doi:10.1007/s10854-024-13671-5.

[2] S. Akshay Kalyan, N. Kanagathara, M. K. Marchewka, J. Janczak, and K. Senthilkumar. Structure, spectroscopy, and theoretical insights on co-crystals of 2,4-diamino-6-methyl-1,3,5-triazine bis(4-aminobenzoic acid) monohydrate as a promising anticancer agent. *Physica B*, 679:415807, 2024. doi:10.1016/j.physb.2024.415807.

[3] A. Barba-Bon, N. I. Gumerova, E. Tanuhadi, M. Ashjari, Y. Chen, A. Rompel, and W. M. Nau. All-inorganic polyoxometalates act as superchaotropic membrane carriers. *Adv. Mater.*, 36(1):2309219, 2024. doi:10.1002/adma.202309219.

[4] A. Blazevic and A. Rompel. The anderson–evans polyoxometalate: From inorganic building blocks via hybrid organic–inorganic structures to tomorrows "bio-pom". *Coord. Chem. Rev.*, 307:42–64, 2016. doi:10.1016/j.ccr.2015.08.002.

[5] O. Büchner. *Münzmetalle mit und in komplexen Anionen: Synthese, Struktur und Eigenschaften*. PhD thesis, Universität Oldenburg, Oldenburg, Germany, 2005. Dissertation, Universität Oldenburg, Dezember 2005.

[6] R. J. Crooks and M. T. Weller. The syntheses and structures of the complex oxide carbonates ba11pd11o20(co3)2 and ba88ni87o156(co3)19. *J. Solid State Chem.*, 128:220–227, 1997. doi:10.1006/jssc.1996.7191.

[7] M. Delferro, C. Graiff, L. Elviri, and G. Predieri. Self-assembly of polyoxoselenitopalladate nanostars $[Pd_{15}(\mu_3\text{-}SeO_3)_{10}(\mu_3\text{-}O)_{10}Na]^{9-}$ and their supramolecular pairing in the solid state. *Dalton Transactions*, 39:4479–4481, 2010. doi:10.1039/C002237G.

[8] M. Ghosh, D. Sorsche, R. B. Ahmed, and M. Anjass. Stabilizing decavanadate cluster as electrode material in sodium and lithium-ion batteries. *ChemSusChem*, 16:e202300631, 2023. doi:10.1002/cssc.202300631. URL https://doi.org/10.1002/cssc.202300631.

[9] I. N. E. H. Guermi, N. E. H. Bensiradj, A. Saal, M. Almi, and M. Nassar. Theoretical approach to the protonation of anderson type polyoxometalates. *Comput. Theor. Chem.*, 1233:114504, 2024. doi:10.1016/j.comptc.2024.114504.

[10] N. I. Gumerova and A. Rompel. Interweaving disciplines to advance chemistry: Applying polyoxometalates in biology. *Inorg. Chem.*, 60(9):6109–6114, 2021. doi:10.1021/acs.inorgchem.1c00125.

[11] N. V. Izarova, N. Vankova, T. Heine, R. Ngo Biboum, B. Keita, L. Nadjo, and U. Kortz. Polyoxometalates made of gold: the polyoxoaurate. *Angew. Chem. Int. Ed.*, 49: 1886–1889, 2010. doi:10.1002/anie.200905566.

[12] N. V. Izarova, M. T. Pope, and U. Kortz. Noble metals in polyoxometalates. *Angew. Chem. Int. Ed.*, 51:9492–9510, 2012.

[13] Y. Kikukawa, K. Ogihara, and Y. Hayashi. Structure transformation among deca-, dodeca- and tridecavanadates and their properties for thioanisole oxidation. *Inorganics*, 3(2):295–308, 2015. doi:10.3390/inorganics3020295.

[14] R. Kipka and H. K. Müller-Buschbaum. Über oxocuprate, xx ein erdalkaliooxocuprat(ii) mit geschlossenen baugruppen: Bacuo2/about oxocuprates, xx alkaline-earth oxocuprate(ii) with closed structural groups: Bacuo2. *Z. Naturforsch*, 32b: 124–126, 1977. doi:10.1515/znb-1977-0201.

[15] A. Klamt. Conductor-like screening model for real solvents: a new approach to the quantitative calculation of solvation phenomena. *J. Phys. Chem.*, 99(7):2224–2235, 1995. doi:10.1021/j100007a062.

[16] A. Kondinski. Metal–metal bonds in polyoxometalate chemistry. *Nanoscale*, 13 (32):13574–13592, 2021. doi:10.1039/D1NR03115H.

[17] A. Kondinski. POMAssembler: A topology-based rigid-block construction code for polyoxometalate architectures. Version 1.0.0. Zenodo, 2026. MIT licence.

[18] A. Kondinski and K. Y. Monakhov. Breaking the gordian knot in the structural chemistry of polyoxometalates: Copper (ii)–oxo/hydroxo clusters. *Chem. Eur. J.*, 23(33):7841–7852, 2017. doi:10.1002/chem.201701040.

[19] A. Kondinski and T. N. Parac-Vogt. Keggin structure, quō vādis? *Front. Chem.*, 6: 346, 2018. doi:10.3389/fchem.2018.00346.

[20] A. Kondinski, N. Vankova, F. Schinle, P. Jäger, O. Hampe, U. Kortz, and T. Heine. How counterions affect the solution structure of polyoxoaurates: Insights from uv/vis spectral simulations and electrospray mass spectrometry. *Eur. J. Inorg. Chem.*, 2014(23):3771–3778, 2014. doi:10.1002/ejic.201402275.

[21] A. Kondinski, A. Banerjee, and S. S. Mal. Hervé- and krebs-type magnetic polyoxometalate dimers. *Magnetochemistry*, 8(9):96, 2022. doi:10.3390/magnetochemistry8090096.

[22] A. Kondinski, A. M. Oyarzún-Aravena, S. D. Rihm, J. Bai, S. Mosbach, J. Akroyd, and M. Kraft. Automated assembly modeling of metal–organic polyhedra. *Eur. J. Inorg. Chem.*, 28(26):e202500115, 2025. doi:10.1002/ejic.202500115.

[23] J.-H. Kruse, M. Langer, I. Romanenko, I. Trentin, D. Hernández-Castillo, L. González, F. H. Schacher, and C. Streb. Polyoxometalate-soft matter composite materials: design strategies, applications, and future directions. *Adv. Funct. Mater.*, 32(51):2208428, 2022. doi:10.1002/adfm.202208428.

[24] O. Linnenberg, A. Kondinski, and K. Y. Monakhov. *The Lindqvist hexavanadate: A platform for coordination-directed assembly*, chapter The Lindqvist hexavanadate: A platform for coordination-directed assembly, pages 39–66. Nova Science Publishers, Hauppauge, NY, 2017.

[25] R. Liu and C. Streb. Polyoxometalate-single atom catalysts (pom-sacs) in energy research and catalysis. *Adv. Energy Mater.*, 11(25):2101120, 2021. doi:10.1002/aenm.202101120.

[26] X. López, P. Miró, J. J. Carbó, A. Rodríguez-Fortea, C. Bo, and J. M. Poblet. Current trends in the computational modelling of polyoxometalates. *Theor. Chem. Acc.*, 128 (4–6):393–404, 2011. doi:10.1007/s00214-010-0820-9.

[27] D. Malcolm and L. Vilà-Nadal. Computational study into the effects of countercations on the polyoxometalate wheel. *ACS Org. Inorg. Au*, 3(5):274–282, 2023. doi:10.1021/acsorginorgau.3c00014.

[28] M. Mirzaei, H. Eshtiagh-Hosseini, M. Alipour, and A. Frontera. Recent developments in the crystal engineering of diverse coordination modes (0–12) for keggin-type polyoxometalates in hybrid inorganic–organic architectures. *Coord. Chem. Rev.*, 275:1–18, 2014. doi:10.1016/j.ccr.2014.03.012.

[29] E. Mohanapriya, S. Elangovan, J. Janczak, K. Sukumar, N. Kanagathara, and V. Ragavendran. Structure, DFT calculations, spectroscopic characterization, and solvent-dependent HOMO-LUMO studies of 3-(hydroxymethyl) pyridinium 4-hydroxybenzenesulfonate. *Mater. Today Commun.*, 41:110632, 2024. doi:10.1016/j.mtcomm.2024.110632.

[30] M. Nyman and P. C. Burns. A comprehensive comparison of transition-metal and actinyl polyoxometalates. *Chem. Soc. Rev.*, 41(22):7354–7367, 2012. doi:10.1039/C2CS35191B.

[31] R. G. Parr and R. G. Pearson. Absolute hardness: companion parameter to absolute electronegativity. *J. Am. Chem. Soc.*, 105(26):7512–7516, 1983. doi:10.1021/ja00364a005.

[32] R. G. Parr and W. Yang. *Density-Functional Theory of Atoms and Molecules*. Oxford University Press, New York, 1989.

[33] R. G. Parr, L. V. Szentpály, and S. Liu. Electrophilicity index. *J. Am. Chem. Soc.*, 121(9):1922–1924, 1999. doi:10.1021/ja984492x.

[34] M. T. Pope and T. F. Scully. Geometrical isomerism arising from partial substitution of metal atoms in isopoly and heteropoly complexes. possibilities for the keggin structure. *Inorg. Chem.*, 14(4):953–954, 1975. doi:10.1021/ic50148a029.

[35] M. T. Pope, Y. Jeannin, and M. Fournier. *Heteropoly and isopoly oxometalates*, volume 8. Springer, 1983.

[36] B. Praveena, T. Sivanesan, N. Kanagathara, R. Ranjani, J. Janczak, and K. Senthilkumar. Growth, structural, spectral, optical, thermal, third-order nonlinear optical characteristics, and DFT studies of morpholinium trichloroacetate–trichloroacetic acid co-crystals for potential optoelectronic applications. *Opt. Mater.*, 149:115066, 2024. doi:10.1016/j.optmat.2024.115066.

[37] B. Praveena, T. Sivanesan, R. Ranjani, J. Janczak, S. Elangovan, A. M. Al-Mohaimeed, M. A. Ali, and N. Kanagathara. Growth, structure, spectral, optical, dielectric, and thermal studies on morpholinium 2,4,6-trinitrophenolate: an organic nonlinear optical crystal. *J. Mater. Sci. Mater. Electron.*, 35:1875, 2024. doi:10.1007/s10854-024-13588-z.

[38] B. Praveena, T. Sivanesan, S. Elangovan, R. Ranjani, K. Sukumar, and E. Mohanapriya. Exploring optical, electronic and NLO properties: Growth and characterization of rubidium hydrogen (+)-tartrate crystals. *Opt. Mater.*, 158:116487, 2025. doi:10.1016/j.optmat.2024.116487.

[39] P. Putaj and F. Lefebvre. Polyoxometalates containing late transition and noble metal atoms. *Coord. Chem. Rev.*, 255(15–16):1642–1685, 2011. doi:10.1016/j.ccr.2011.01.030.

[40] C. C. Pye and T. Ziegler. An implementation of the conductor-like screening model of solvation within the amsterdam density functional package. *Theor. Chem. Acc.*, 101(6):396–408, 1999. doi:10.1007/s002140050457.

[41] SCM, Theoretical Chemistry. Adf 2017.113, 2017. Amsterdam Modeling Suite program package; available online at https://www.scm.com.

[42] A. Solé-Daura, J. M. Poblet, and J. J. Carbó. Structure-activity relationships for the affinity of chaotropic polyoxometalate anions towards proteins. *Chem. Eur. J.*, 26 (26):5799–5809, 2020. doi:10.1002/chem.201905533.

[43] X.-F. Su, B. Zhu, L. Liu, L.-K. Yan, and Z.-M. Su. DFT characterization on the effect of redox-inactive cation Ca^{2+} on water oxidation by Co^{II}-based cuboidal catalyst. *Computational and Theoretical Chemistry*, 1152:1–6, 2019. doi:10.1016/j.comptc.2019.01.023.

[44] G. t. Te Velde, F. M. Bickelhaupt, E. J. Baerends, C. Fonseca Guerra, S. J. van Gisbergen, J. G. Snijders, and T. Ziegler. Chemistry with adf. *J. Comput. Chem.*, 22 (9):931–967, 2001.

[45] S. Van Gisbergen, J. Snijders, and E. Baerends. Implementation of time-dependent density functional response equations. *Comput. Phys. Commun.*, 118(2-3):119–138, 1999. doi:10.1016/S0010-4655(98)00252-8.

[46] E. Van Lenthe and E. J. Baerends. Optimized slater-type basis sets for the elements 1–118. *J. Comput. Chem.*, 24(9):1142–1156, 2003. doi:10.1002/jcc.10255.

[47] E. van Lenthe, E.-J. Baerends, and J. G. Snijders. Relativistic total energy using regular approximations. *J. Chem. Phys.*, 101(11):9783–9792, 1994. doi:10.1063/1.467940.

[48] E. Van Lenthe, A. Ehlers, and E.-J. Baerends. Geometry optimizations in the zero-order regular approximation for relativistic effects. *J. Chem. Phys.*, 110(18):8943–8953, 1999. doi:10.1063/1.478813.

[49] V. Vijayalakshmi, N. Kanagathara, J. Janczak, M. K. Marchewka, M. Azam, and K. Senthilkumar. Structural, spectroscopic and second harmonic generation evaluation of 1,2,4-triazolinium tartrate–tartaric acid as a promising nonlinear optical material. *Opt. Mater.*, 147:114694, 2024. doi:10.1016/j.optmat.2023.114694.

[50] V. Vijayalakshmi, N. Sivakumar, V. Ali Alsulmi, S. Elangovan, N. Kanagathara, and J. Janczak. Exploring structure, molecular interactions, optical and thermal properties of Bis(2-Aminopyrimidinium) selenate monohydrate: A combined experimental and theoretical study. *Opt. Mater.*, 152:115539, 2024. doi:10.1016/j.optmat.2024.115539.

[51] Y. Xiang, N. V. Izarova, F. Schinle, O. Hampe, B. Keita, and U. Kortz. The selenite-capped polyoxo-4-aurate(iii). *Chem. Commun.*, 48:9849–9851, 2012. doi:10.1039/C2CC33795A.

[52] F. Xu, H. N. Miras, R. A. Scullion, D.-L. Long, J. Thiel, and L. Cronin. Correlating the magic numbers of inorganic nanomolecular assemblies with a Pd84 molecular-ring rosetta stone. *Proc. Natl. Acad. Sci. U.S.A.*, 109(29):11609–11612, 2012. doi:10.1073/pnas.1202981109.

[53] P. Yang and U. Kortz. Discovery and evolution of polyoxopalladates. *Acc. Chem. Res.*, 51(7):1599–1608, 2018. doi:10.1021/acs.accounts.8b00082.

[54] J. Zhang, Y. Huang, G. Li, and Y. Wei. Recent advances in alkoxylation chemistry of polyoxometalates: From synthetic strategies, structural overviews to functional applications. *Coordination Chemistry Reviews*, 378:395–414, 2019. doi:10.1016/j.ccr.2017.10.025.